Journal of Geophysical Research: Solid Earth

RESEARCH ARTICLE
10.1029/2018JB015635

Key Points:
- Near-source ground motion presents directive impulsive signals occurring on average at ~12% of receivers around the source
- Pulse occurrence and duration are enhanced on the footwall of the fault, as compared to the hanging wall
- Pulse occurrence and duration mainly depend on the rupture speed, average risetime, and hypocenter depth

Supporting Information:
- Supporting Information S1

Correspondence to:
A. Scala,
antonio.scala@ingv.it

Citation:
Scala, A., Festa, G., & Del Gaudio, S. (2018). Relation between near-fault ground motion impulsive signals and source parameters. *Journal of Geophysical Research: Solid Earth*, *123*, 7707–7721. https://doi.org/10.1029/2018JB015635

Received 8 FEB 2018
Accepted 4 AUG 2018
Accepted article online 14 AUG 2018
Published online 7 SEP 2018
Corrected 24 JAN 2019

This article was corrected on 24 JAN 2019. See the end of the full text for details.

Relation Between Near-Fault Ground Motion Impulsive Signals and Source Parameters

A. Scala[1,2], G. Festa[2], and S. Del Gaudio[2,3]

[1]Istituto Nazionale di Geofisica e Vulcanologia - Sezione Roma 1, Rome, Italy, [2]Dipartimento di Fisica "Ettore Pancini" - Università degli studi di Napoli Federico II, Naples, Italy, [3]Now at Stogit S.p.A., via Libero Comune, Crema, Italy

Abstract Near-fault ground motion records often present impulsive signals, characterized by a large amplitude in the velocity wavefield and by the energy concentrated in a short time window as compared to the total earthquake duration. This *pulse-like* behavior is ascribed to the directivity of the seismic rupture, and it requires a stronger demand to the buildings not predicted by the classical design spectra. In this work we investigate the pulse occurrence and duration in near-fault synthetic seismograms generated from an ensemble of k^{-2} source models. We exploited the fault geometry of the M_w = 6.3, 2009 L'Aquila earthquake, which represents a typical example of normal-fault earthquake for which several records in the fault vicinity are available for comparison with synthetics. We show that impulsive records are sensitive to the rupture velocity, to the hypocenter depth, and to the station location, whether it is on the hanging wall or on the footwall. The pulse duration was also shown to be proportional to the risetime, and it scales with the source-receiver distance and inversely with the rupture velocity. We model these results as an effect of the coupled along-strike and updip directivity.

1. Introduction

Ground motion and its variability are influenced to the first order by earthquake source and wave propagation effects, the latter occurring at crustal and local scales. Fault mechanism, radiation pattern, and directivity are the main source effects that may change the amplitude and the shape of the waveforms as a function of the source azimuth, at the same distance from the source. These effects have been theoretically and numerically analyzed (Bernard & Madariaga, 1984a, 1984b; Hanks & McGuire, 1981; Somerville et al., 1997), and they are empirically retrieved to influence the ground motion; they affect the attenuation relationships, both for peak values and spectral ordinates (e.g., Akkar & Bommer, 2010; Spudich & Chiou, 2008).

Classical along-strike rupture directivity enhances the *S* wave amplitude up to a factor of 10 in the direction of the rupture propagation, for strike-slip events (Bernard et al., 1996; Boatwright & Boore, 1982). However, a rupture developing along normal and thrust faults that nucleates at depth can interact with the free surface and can also produce along-dip (updip) directivity in the near source region (Sommerville, 2005). Such ruptures can mechanically accelerate to the *S* wave speed in the along-strike, antiplane direction while either they are limited to the Rayleigh wave speed (subshear regime) or they can accelerate toward the *P* wave velocity (supershear regime) along the updip, in-plane direction (Burridge, 1973; Rice, 1979). For these ruptures, the situation is reversed as compared to strike-slip events, and they are expected to mechanically enhance the ground motion in the near-source domain, in the along-dip direction.

Such theoretical expectation was also observed in real data recorded during normal/thrust events, resulting in pulses at stations located in the hanging wall and footwall of the fault, in the source vicinity (Chioccarelli & Iervolino, 2010). These pulses dominate the velocity wavefield of near-source stations; they are concentrated in the initial portion of the signal and they are characterized by a short duration and a relevant amplitude with respect to the average amplitude, as inferred from ground motion prediction equations (Baker, 2007; Somerville et al., 1997).

With the increase of the densification of accelerometric networks surrounding active faults, pulse-like signals are nowadays recorded for a wide class of events. Also, recent normal earthquakes in Italy, such as the 1997, *M* 6.0 Colfiorito, the 2009, *M* 6.3 L'Aquila, the 2016, *M* 6.0 Amatrice, and the 2016, *M* 6.5 Norcia earthquakes, clearly generated pulse-like signals (Chioccarelli & Iervolino, 2010; Cultrera et al., 2009; Iervolino et al., 2016, 2017).

Numerical algorithms have been designed to retrieve pulses from the three-component ground motion records, based on wavelet analysis (Baker, 2007; Baker et al., 2011). Using these algorithms, the pulses from strike-slip events are predominantly observed on the fault-normal component of the ground velocity records (Somerville et al., 1997), while there is a large variability in the orientation of near-source pulses for dip slip events (Luzi et al., 2016). Additionally, pulse duration is comparable or slightly larger than the average rise-time of the source, although its distribution exhibits a large intraevent variability (Baker, 2007). Several studies have been performed to show its dependence on the magnitude (Baker, 2007; Bray & Rodriguez-Marek, 2004; Mavroeidis & Papageorgiou, 2003; Sommerville, 2003) and on other source parameters such as the hypocentral position and the rupture velocity (Fayjaloun et al., 2017; Mavroeidis & Papageorgiou, 2010). Some authors also claim a dependence on the remote stress field and tectonic regime (Cork et al., 2016).

The signature of rupture directivity in the ground-motion signals has been often used to constrain the source models (Abercrombie et al., 2017; Luo et al., 2010) and to detect a preferred rupture propagation direction associated with geometrical discontinuities (Calderoni et al., 2015) of the fault and/or with bimaterial propagation (Kane et al., 2013; Rubin & Ampuero, 2007; Scala et al., 2017).

However, a more comprehensive understanding of the impulsive ground motion characteristics and their connection to the seismic source features still require further analysis.

The pulse-like signal behavior requires a stronger demand to the buildings affecting the spectral shape of the expected ground motion (Iervolino & Cornell, 2008). Specifically, the elastic demand in the presence of pulses is expected to be larger than for nonpulse signals and developed in a short time window, with an increase of the spectral ordinates near the pulse period (Alavi & Krawinkler, 2001; Hubbard & Mavroeidis, 2011; Liossatu & Fardis, 2016; Ruiz-Garcia, 2011; Tothong & Luco, 2007). The inelastic demand has been shown to affect the spectral ordinates at periods smaller than half of the pulse period (Baltzopoulos et al., 2016; Iervolino et al., 2012). Indeed, probabilistic hazard analysis may fail to provide accurate estimates of response spectra in the near source range, for fault mechanisms and locations that favor the emergence of pulses (Chioccarelli & Iervolino, 2013; Tothong et al., 2007). Therefore, some algorithms to include directivity in probabilistic seismic hazard assessment have been recently proposed (Shahi & Baker, 2011). On the other hand, including directivity effects in the definition of attenuation laws contributes to reduce their uncertainties (Kurzon et al., 2014).

In this study we analyze how source parameters affect the pulse occurrence and its variability. Fayjaloun et al. (2017) investigated the intraevent variability of the pulse, in terms of pulse period. They showed that the source-station geometry and the rupture speed are the main factors that affect the pulse duration, which can be as large as 8–10 s for a magnitude 6.5 event.

In this study, we thoroughly investigated the pulse occurrence, using a kinematic description of the rupture and we analyzed how the kinematic source parameters affect the pulse occurrence and its duration. In the next section we describe the numerical simulations used to generate near-source strong motion synthetics from a kinematic description of the rupture. Then we discuss how the pulse is detected and characterized in terms of its duration. We discuss the parameter dependence and their mutual correlation on the pulse occurrence. We finally evaluate the intraevent variability associated with the pulse occurrence and compare it to the variability observed in the empirical relationships.

2. Numerical Simulations of Pulse-Like Signals

To address the role of the source parameters in the pulse occurrence and its duration, we produced several sets of synthetic seismograms in the geometrical configuration of the L'Aquila earthquake. This event represents a typical normal fault earthquake for Italy in terms of geometry and size, for which several pulse-like signals were observed (Chioccarelli & Iervolino, 2010). Additionally, the wide literature on this earthquake and the availability of several near-source strong motion data allow to put constraints on source geometry and kinematics and to compare the results from simulations with the recorded waveforms. For this study, the geometry, the moment magnitude, and the station distribution were indeed fixed to the ones of the L'Aquila event. We modeled a M_w 6.3 earthquake, along a normal fault striking at 135° and dipping at 50° (Chiarabba et al., 2009). Fault length and width are, respectively, L = 28 km and W = 22 km (Cirella et al., 2009). To investigate the sensitivity of the kinematic source parameters to the pulse occurrence and duration,

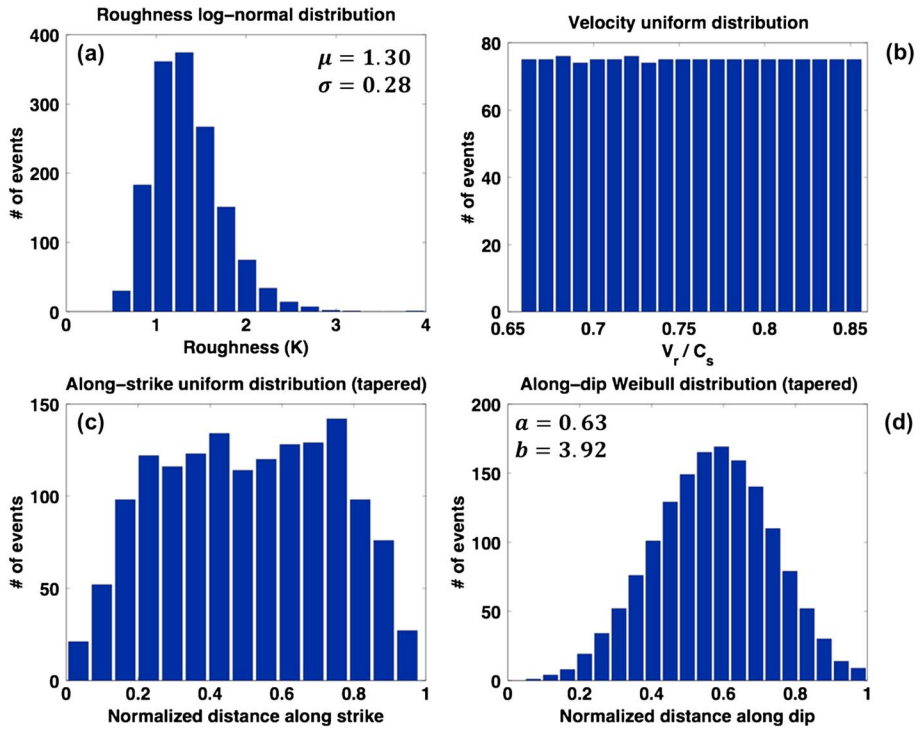

Figure 1. Number of events as a function of the source parameters. (a) Lognormal distribution of roughness *K*. (b) Uniform distribution of rupture velocity between 65% and 85% of *S* wave velocity. (c) Uniform distribution of the nucleation position with respect to the strike direction; the distribution is tapered at the boundaries of the domain. (d) Weibull distribution of the nucleation depth as a function of the along-dip distance.

we allowed the position of hypocenter, the rupture velocity, the risetime, and the slip distribution to vary on the fault plane.

We modeled the seismic source adopting a kinematic k^{-2} model that describes the f^{-2} high-frequency decay observed in the far-field displacement spectra (Causse et al., 2009; Herrero & Bernard, 1996). According to this model, slip distributions are represented in the wave number domain $\mathbf{k}$ by a $|\mathbf{k}|^{-2}$ decay beyond the corner wave number k_c, where $k_c = K/L_C$, K represents the dimensionless roughness parameter, and L_c represents the smallest fault dimension, that is in this case the fault width W. Therefore, K is inversely proportional to the size of the main asperity of the slip over the fault plane (Causse et al., 2009; Del Gaudio et al., 2015). The rupture evolution on the fault was modeled as a slip pulse of width L_0, related to the average risetime, and propagating at constant rupture velocity V_r from the hypocenter. The synthetic seismograms were computed assuming a 1-D velocity model for wave propagation (Bianchi et al., 2010 modified by Ameri et al., 2012). Numerical Green's tractions were evaluated for each subfault station couple and for 181 frequency values ranging from 0.05 to 2.2 Hz, the latter value being the maximum deterministic frequency in the simulations. We used the software AXITRA for the computation of the Green's functions (Coutant, 1989). The seismic signals were finally enriched in high frequency (up to 25 Hz) by adding a stochastic contribution to fit the Peak Ground Acceleration (PGA) and the Arias intensity according to the ground motion prediction equations of Sabetta and Pugliese (1996). The coupling with the deterministic numerical part of the seismograms was done using matched filters in the frequency domain (Smerzini & Villani, 2012).

The K parameter for the simulations was extracted from a lognormal distribution (Causse et al., 2009). While its standard deviation was fixed to 0.28 (Del Gaudio et al., 2015), we analyzed two different cases for the mean value of K, $\mu_K = 0.74$, and $\mu_K = 1.3$. The lowest value corresponds to have self-similar ruptures at all scales, from the aftershocks to the main event (Causse et al., 2009). Maintaining fixed the event magnitude, larger values of the roughness parameter correspond to concentrate the slip in patches of smaller size. Kinematic models of the L'Aquila earthquake effectively show slip concentration in patches whose size is smaller than the width of the fault (Cirella et al., 2009; Del Gaudio et al., 2015; Gallovic & Zahradnik, 2011). Indeed, larger

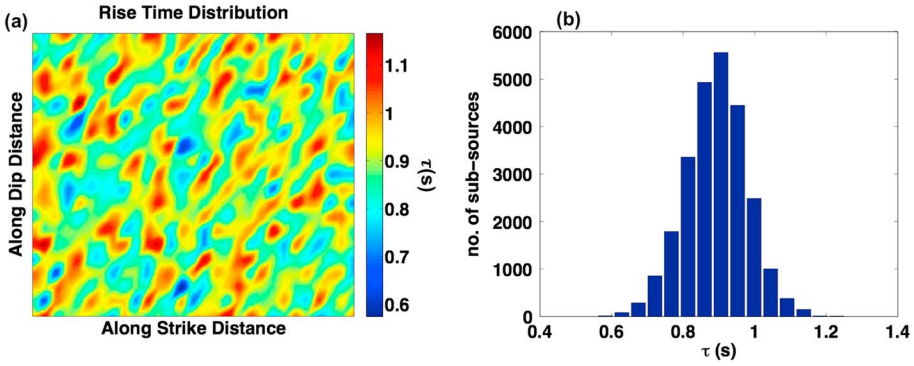

Figure 2. (a) Example of distribution of risetime on the fault plane with an average risetime $\tau = 0.9$s. (b) Histogram of the risetime Gaussian distribution.

values of K were also tested to investigate the effect of small patches on the generation of pulse signals. In Figure 1a the roughness distribution for an ensemble of 1,500 source models, with mean value equal to 1.3, is shown. Figure S1 of the supporting information shows three different slip distributions obtained from three different K values as extracted from the distribution of Figure 1a.

The rupture velocity for each simulation was chosen to be constant, with values extracted from a uniform distribution limited between 65% and 85% of the S wave velocity, the latter quantity being evaluated in the near-fault region (Figure 1b). This choice is justified by the seismological evidence of the fast acceleration of the rupture toward the limit rupture velocity (Mai & Thingbaijam, 2014), which is the Rayleigh wave speed for subshear in-plane ruptures and the S wave speed for antiplane ruptures.

Hypocenter position along strike was extracted from a uniform distribution tapered at the edges of the fault plane, whereas its position along dip was assumed to follow a Weibull distribution to ensure that a deep nucleation is more likely to occur than a shallow one (Causse et al., 2009). These two distributions are shown in Figures 1c and 1d. In these plots, the distance along strike, from north-west to south-east, is normalized to the fault length L whereas that distance along the dip, from north-east to south-west, is normalized to the fault width W. The 1,500 different source models are defined extracting parameters from the distributions showed in Figure 1.

The average risetime was selected according to the values expected for an M_w 6.3 event. According to the scaling laws in literature, we have $0.5\ \text{s} \leq \tau \leq 1.0\ \text{s}$ for events of magnitude between 6.0 and 6.5 (Geller, 1976; Sato, 1979). We assumed values varying between 0.6 and 1.2 s, the minimum value being constrained by the maximum frequency deterministically simulated in the numerical Green's tractions. We performed simulations both with constant and variable risetime on the fault plane. In this latter case, we extracted a value for each subfault from a Gaussian distribution with standard deviation of 0.1 s, while the range of the mean value is the same as for the constant case. Also, for a variable risetime, the distribution of risetime was forced to maintain a spatial coherence between contiguous subsources.

An example of variable risetime distribution (with mean value $\overline{\tau} = 0.9\,\text{s}$) on the fault plane is shown in Figure 2a, with the associated histogram represented in Figure 2b.

For the first part of the analysis, we selected four stations, where real accelerograms are also available. Three of them (AQU, AQK, and AQG) are located on the surface projection of the fault plane and thus on the hanging wall; the fourth station (GSA) is outside this projection, on the footwall, at a distance from the M_w 6.3 L'Aquila earthquake epicenter of about ~25 km. This choice will allow to compare the pulse occurrence both in the synthetic and real data in order to validate the numerical simulations. To analyze the spatial distribution of impulsive ground motion records, more stations were added as shown in Figure 3. In this plot the real stations are represented in orange and the additional stations in blue.

The station distribution is symmetric with respect to the dip direction, and the receivers cover pretty uniformly the near-fault area. As shown in section 5, this allows for an estimation of the intraevent spatial variability in terms of percentage of near-source stations subjected to an impulsive ground shaking.

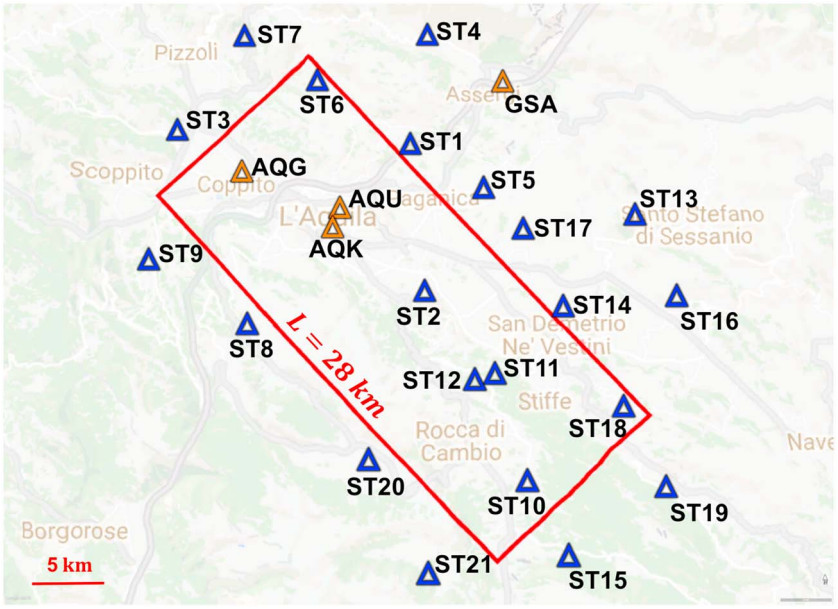

Figure 3. Station distribution used for the simulations. Orange triangles represent the position of the real stations. Blue triangle stations were added to study the spatial distribution of the pulse occurrence and duration. Red rectangle represents the projection of the fault on the surface. The along-strike length was assumed 28 km, whereas the along dip width is 20 km (Cirella et al., 2009). The shallowest point of the fault is at 500-m depth, whereas the deepest point is at 16.7-km depth. Strike angle is imposed at 130°, and the dip angle is at 50° (Chiarabba et al., 2009).

The space scale associated with the average interstation distance is able to capture the space variability of the pulse occurrence for this simplified source model. A denser station distribution would require a more detailed description of the source geometry including possible variations in the focal mechanism during the rupture propagation and small-scale complexities in the rupture kinematics.

2.1. Pulse Detection

The pulses were detected and characterized by a wavelet analysis (Baker, 2007). For each three-component waveform, the two horizontal traces were transformed using a Daubechies wavelet transform of order 4. The signals were then rotated in the horizontal direction that maximizes the pulse amplitude. This procedure is different from the classical one adopted to seek for pulses, which is limited to the analysis of the fault-normal component in the data (Baker, 2007; Chioccarelli & Iervolino, 2010; Somerville et al., 1997). Indeed, here we want to identify the features of the largest amplitude impulsive signals that may occur along directions different from the fault-normal one.

After rotating the trace in the direction that maximizes the pulse (Figure S2a of the supporting information), the pulse given by the wavelet transform (Figure S2b) is subtracted from the original signal to compute the residual ground motion (Figure S2c). Finally, the pulse indicator (*Pi*) is computed as follows (Baker, 2007):

$$Pi = \frac{1}{1 + e^{-23.3+14.6(\mathrm{PGV_{ratio}})+20.5(\mathrm{E_{ratio}})}} \tag{1}$$

where $\mathrm{PGV_{ratio}}$ is the ratio between the peak ground velocity (PGV) measured on the residual trace and the PGV measured on the original rotated signal. Analogously, the energy ratio E_{ratio} is the ratio between the energy computed on the same two traces, where the energy is defined as the integral of the squared velocity. As suggested by Baker (2007), potential pulses have to verify the condition $Pi > 0.85$. Two further conditions are considered to classify a signal as impulsive. First, the PGV on the original trace must be larger than 20 cm/s. This choice avoids that relatively low amplitude signals are recognized as pulse-like records because the velocity time history has a simple shape in our synthetics (Baker, 2007). Moreover, pulse-like signals are associated to the direct *S* wave. Indeed, we also require that the time, at which the energy of the original trace is reduced to the 20% of its value, is larger than the time at which the energy of the detected pulse is reduced

at the 10% of its value. Although there is no unambiguous definition for the period from the wavelet analysis, the comparison of the maximum of the wavelet Fourier spectrum with a sine wave having the same period allows to extract a pulse pseudoperiod. This pseudoperiod provides an estimation of the duration of the pulse (Baker, 2007). We noticed that during the analysis a few pulses emerged with duration of about 0.5 s. This period is close to the inverse of the maximum frequency associated with the deterministic contribution to the numerical simulations (2.2 Hz). Inspecting the corresponding pulses, we found that these pulses were generated by spurious amplifications in the stochastic high-frequency contribution. After discarding these spurious impulsive signals, we found that the remaining pulses all have a duration larger than 1.0 s. We also verified that the pulse emergence is robust independent of the stochastic contribution. When fixing the deterministic part of an impulsive signal, in all cases the pulse emerges in more than 85% of synthetic signals obtained by changing the stochastic contribution.

3. Impulsive Signals at Real Stations

3.1. Pulse Occurrence

As a first analysis, we compared the results related to the frequency of pulse occurrence obtained with constant and variable risetime. In the comparison, the mean of the Gaussian distribution producing a variable risetime is the same as the constant risetime value. In Figure 4a the histograms for pulse occurrence are shown at the four stations separately (first four bars from left) and when merging all the synthetic traces together (last bar on the right) both for a constant risetime $\tau = 0.6$ s (blue bars) and for a variable risetime with a mean value of $\bar{\tau} = 0.6$ s (red bars). Both histograms result from 1,500 simulations. Figure 4a shows that the pulse occurrence is almost insensitive to the risetime distribution on the fault, when fixing the mean value and the pulse occurs slightly more frequently in the case of constant risetime (~1%). The same results hold for all the investigated risetime values, showing that an inhomogeneous risetime poorly differentiates from a constant one for the probability of the pulse emergence. This conclusion allows us to assume hereinafter a constant risetime. Nevertheless, the absolute value of the risetime strongly affects the emergence of the pulse and its frequency increases when increasing the risetime value as shown in Figures 4b and 4c where the histograms of the pulse occurrence are shown for $\tau = 0.9$ and 1.2 s, respectively. The increasing probability of occurrence is more pronounced for the stations on the hanging wall than for GSA, located on the footwall. The larger the risetime the larger the portion of the fault that emits coherently.

For the different risetime distributions, 1,500 source models are generated, and the associated synthetics are calculated. In order to understand how the single source parameters may affect the generation of impulsive records, the source parameters are clustered in equally spaced bins; within each bin the ratio between the number of events presenting pulse over the total number of events is used to provide an estimate of the probability of occurrence of the pulse itself. Thus, this ratio represents the marginal probability of the pulse occurrence for that single parameter, obtained after integration over the whole variability domain for the other parameters. As concerns the rupture velocity, the fraction of impulsive events almost linearly increases with the rupture speed, for all the analyzed stations, as shown in Figure 5a. We recognize a similar trend at stations AQK, AQU, and GSA, while the increase is less evident at station AQG. Nevertheless, the limited number of impulsive signals recorded at this station makes the statistics less robust than at other stations. The increasing probability of the pulse occurrence with the increase of the rupture velocity (or the risetime) can be associated with the directivity effect: the faster the rupture, the shorter the radiation time from slip patches.

A similar analysis was carried out for the hypocenter depth as shown in Figure 5b. The percentage of pulse-like signals exhibits a saturation at an intermediate depth for GSA while it is an increasing function of the depth for AQU and AQK. Again, the small number of pulses at AQG does not allow to evidence any trend for this station. The increasing pulse emergence with depth is a signature of the updip directivity. For GSA, beyond the saturation depth (at about 0.6 times the maximum depth) we do not observe any further increase of the number of pulses; since the footwall station experiences updip directivity all along the dip section of the fault, this length scale defines a characteristic directive updip length required to generate pulses at this station.

When the pulses are analyzed as a function of the roughness (Figure 5c), we found a maximum for the pulse occurrence at GSA, AQK, and AQU between $K = 0.9$ and $K = 1.1$. These results hold independently of the mean

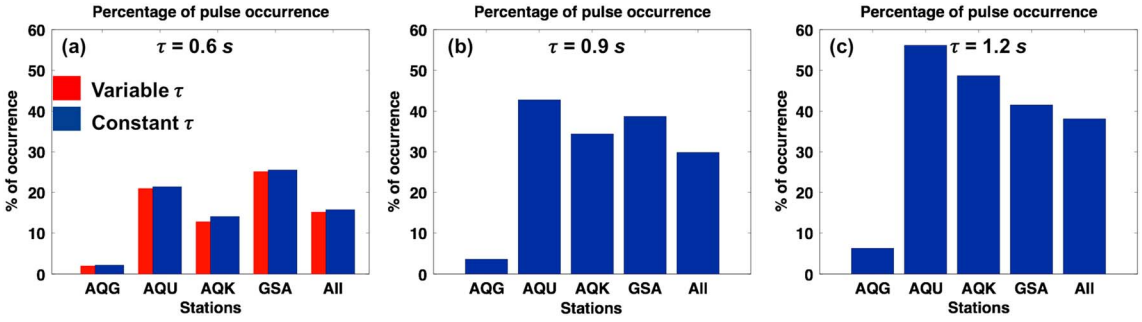

Figure 4. Comparison between the histograms related to the occurrence of the pulse for each station (first four bars from left) and merging all the traces from all the stations (last bar). They are represented for different constant values of risetime: (a) $\tau = 0.6$ s; (b) $\tau = 0.9$ s; (c) $\tau = 1.2$ s. In Figure 4a the percentage of pulse occurrence is also shown for a variable risetime normally distributed around the average value $\bar{\tau} = 0.6$ (red bars). This latter comparison is shown to demonstrate the equivalence between a constant and a variable risetime distribution in terms of pulse occurrence.

value of roughness, whether it is 0.74 or 1.3. When the parameter $K \approx 1$, the size of the main slip asperity is comparable with the width of the fault and this appears to be the favored condition to generate impulsive behavior in the ground motion. Smaller values of K smoothen more and more the slip originating smaller amplitude signals, whereas higher values of K concentrate the slip in smaller size patches making the rupture propagation less coherent and limiting the directivity effect and thus the pulse emergence. Since we have verified that the mean value of the roughness distribution does not produce significant effects on the pulse occurrence; hereinafter, we present results achieved using a lognormal distribution with mean $\mu_K = 0.74$. Finally, the marginal probability density function for the along-strike coordinate of the position of hypocenter shows that the number of pulse events increases with the increasing distance from the station toward south-east (see Figure 5d) as a signature of the along-strike directivity, up to a maximum of

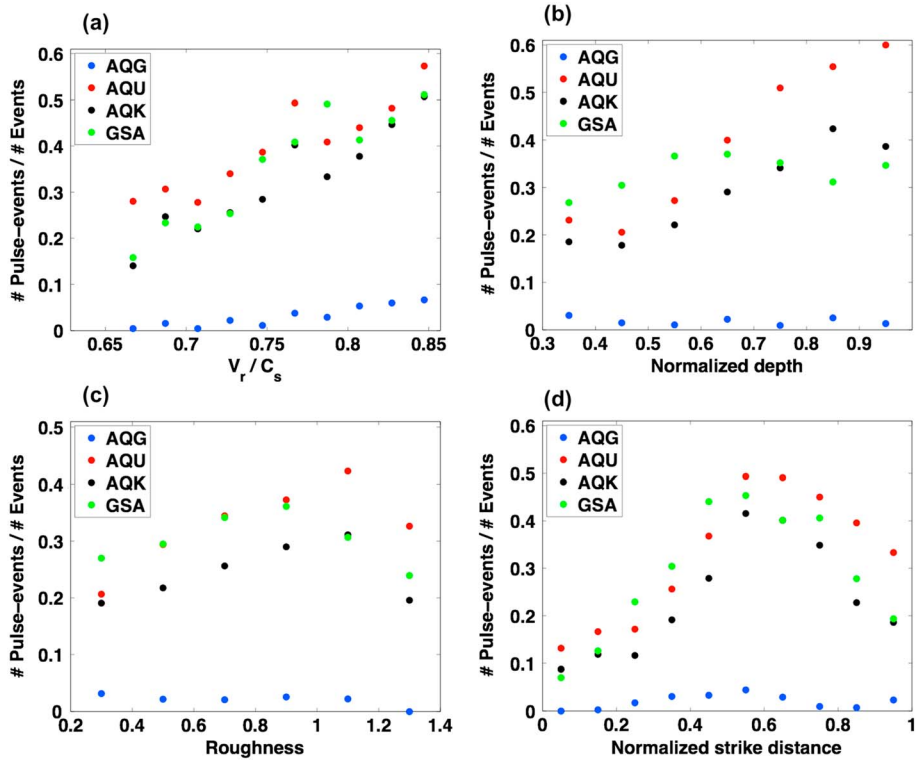

Figure 5. The number of events with pulses over total number of events is used to provide an estimate of the marginal probability of pulse occurrence as a function of the single source parameters. The ratio is shown as a function of rupture velocity (a), normalized along-dip hypocenter position (b), roughness (c), and along-strike hypocenter position (d).

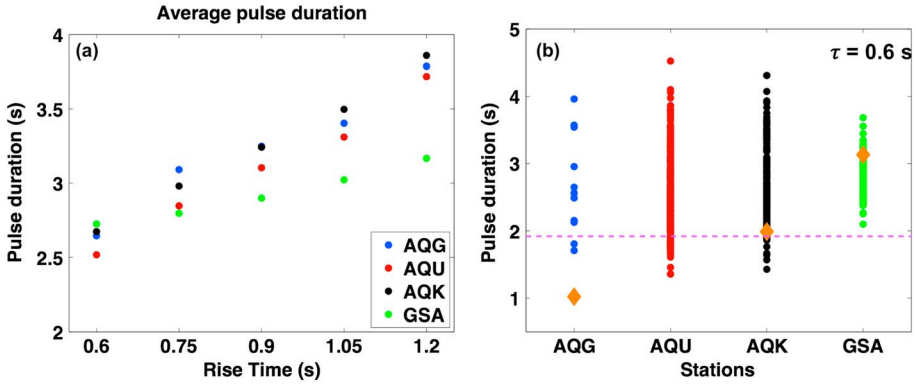

Figure 6. Variability of pulse duration as a function of the risetime for the four stations: (a) the average of pulse duration for each station for increasing risetime. The pulse duration appears to linearly increase as a function of the risetime with stronger dependence for hanging wall stations. (b) For each station and for risetime $\tau = 0.6$ *s*, the different pulse durations are plotted. The orange diamonds reflect the duration of pulses recorded during L'Aquila earthquake (Chioccarelli & Iervolino, 2010), whereas the magenta dashed line represents the expected duration from the magnitude-pulse size scaling law proposed by Baker (2007).

about 0.6 times the fault length. Beyond this maximum the fraction of pulse-like signals decreases. For a small along-strike hypocentral distance, the along-strike directivity contributes to generate a pulse in the first *S* wave arrivals. For longer along-strike distances the directive pulse is delayed with respect to the first *S* wave arrivals and the energy contribution of the pulse, as defined in equation (1), is now concentrated in the middle of the signal. These signals do not satisfy the pulse criterion defined in section 2 and are not recognized as pulses.

The number of pulses observed at the station AQG is small, despite its location on a side of surface projection of the fault would favor the emergence of along-strike directive effects. However, the projection of the station on the fault is at depth and this limits the effect of the updip directivity.

Additionally, since the station is close to the north-west boundary of the fault surface, the seismic waveforms at this station are influenced by stopping phases, which spread the energy within the whole *S* wave packet.

Finally, a two-point correlation analysis was performed to analyze the correlations between the source parameters. The results for AQK are summarized in Figure S3 of the supporting information. They show that large risetime values can generate impulsive signals also for slower (Figure S3a) and shallower ruptures (Figure S3b), whereas no correlation appears between the risetime and the roughness. Analogous correlation can be observed between depth and rupture velocity with increasing probability of pulse occurrence for slower events originating deeper on the fault (Figure S3d). The correlation images show some maxima, in risetime versus rupture velocity and depth versus rupture velocity plots. They do not correspond to a general trend; they are rather specific to single stations. The same two-point correlation analysis was carried out for the station GSA on the footwall (Figures S4a–S4d in the supporting information). For that station the source parameters are poorly correlated with each other, and no clear trends are evidenced.

3.2. Pulse Duration

The analysis was completed with a comparison between distribution of the pulse duration from synthetics and the duration of the impulsive signals recorded during the $M_w = 6.3$ L'Aquila earthquake. We show in Figure 6a that the average value of the duration is an increasing function of the risetime τ. The increase is faster for stations on the hanging wall, whereas the duration at GSA seems to be less influenced by the risetime. The interevent distribution of the duration for the smallest value of the risetime ($\tau = 0.6$ s) is shown in Figure 6b to compare our results with real data and with the duration expected by the Baker classification (Baker, 2007). For AQG only 11 impulsive signals were detected, and their duration oscillates between 1.7 s and 3.6 s, while a pulse of duration 1.02 s was observed at this station (orange diamond on the AQG column in Figure 6b, Chioccarelli & Iervolino, 2010). However, we never found physical pulses with such small durations at AQG and the limited number of pulses makes the statistics not robust. At the other two hanging wall

stations a considerable number of pulses was detected: 326 for AQU (red dots) and 198 for AQK (black dots). These signals show similar behavior in terms of pulse durations, respectively, ranging from 1.4 s to 4.5 s and from 1.4 s to 4.3 s, respectively. In the real data an impulsive ground motion was evidenced only at AQK with a duration of 1.99 s, this value being represented by the orange diamond on the AQK column in Figure 6b (Chioccarelli & Iervolino, 2010). It is compatible with the range derived from simulations. The expected value from the Baker magnitude-pulse size scaling law (1.91 s), and marked with a magenta dashed line in Figure 6b, is also shown to be compatible with the real and the simulated results. Finally, at GSA 397 impulsive signals were recorded with a smaller variability and values ranging from 2.1 to 3.7 s. All these values are larger than the expected value from the Baker scaling law but they fit the real duration (3.13 s), as computed by Chioccarelli and Iervolino (2010) and shown in Figure 6b. When adopting kinematic source models for the L'Aquila earthquake inferred from strong motion and geodetic data (Ameri et al., 2012; Cirella et al., 2012; Del Gaudio et al., 2015), the duration of the pulses (Evangelista et al., 2017) is compatible with the intervals represented in Figure 6b.

4. Spatial Distribution of the Pulses

In order to investigate the spatial distribution of the pulses observed in the near-source region of the L'Aquila-like event, we also computed synthetics seismograms at a larger number of stations located within and around the surface projection of the fault plane. In order to have an almost uniform coverage of the investigated area and to also include the real stations, we compute the ground motion at 25 stations (Figure 3). The station distribution is symmetric with respect to the along-dip direction of the fault. Since the two close stations AQU and AQK show quite similar results, we have not considered the results from AQK and its symmetric station ST12, to keep an almost constant interstation distance.

We already observed (e.g., Figure 4a for risetime $\tau = 0.6$ s) that the footwall station GSA shows a larger probability of pulse occurrence, in spite of the larger distance from the fault plane. When closer stations are considered on the footwall, this large probability of pulse occurrence becomes more evident. Figure 7 shows the pulse occurrence in a synthetic data set of 1,500 scenarios generated from the same source models as used in the previous section and a risetime value of $\tau = 0.6$ s. In Figure 7, the stations on the hanging wall are represented by blue bars and the stations on the footwall are represented by red bars, respectively. Looking at the pulse occurrence on the footwall, the stations ST4 and ST5 and their symmetric ST16 and ST17 show a high percentage (~ 50%) of pulse occurrence; the stations ST1 and ST14, which are closer to the fault boundary, show a lower probability, although this value is still larger than the average probability of pulse occurrence on the hanging wall. Here at stations located between the center of the fault plane projection and north-west and south-east fault boundaries (e.g., AQU and ST11, respectively) the development of pulses is favored as compared to stations close to the boundary (e.g., AQG) and to those located in the middle of the fault projection (e.g., ST2). As expected, the along-strike geometrical symmetry of the station distribution is retrieved in Figure 7 where symmetric stations show very similar probabilities to develop pulses. Exploiting this symmetry, we searched for common source features in the ensemble of the events generating pulse at the same group of stations. In particular, in Figure 8a we show the epicenters of the events (cyan stars) that produce pulses only at the footwall stations ST4-ST5. We can individuate two clusters of events: most of them nucleated on the same fault half-side as the stations at depths between 0.6 W and 0.9 W and produce pulses as a result of pure updip directivity. Most of the remaining events originated on the other half-side of the fault at shallower depths (between 0.5 W and 0.8 W), and the associated pulses result from combined along-strike/along-dip directivity effects. Conversely, when we consider the events producing pulses at one station on the hanging wall (e.g., AQU) and one station on the footwall (e.g., ST4), the epicenter distribution (red stars in Figure 8a) evidence the importance of the contribution of the along-strike directivity to the pulse occurrence. Finally, in all cases, the events that produce pulses at a specific set of stations are clustered on the fault.

Complementarily, we analyzed the number of stations showing a pulse for each event. The results are summarized in the histogram of Figure 8b. Few events do not generate any pulse (~8%), whereas ~46% of the earthquakes generate impulsive signals either at 1 or 2 stations over 23, corresponding to a fraction of stations smaller than the 10%. The remaining part of the events produces pulses at three or more stations

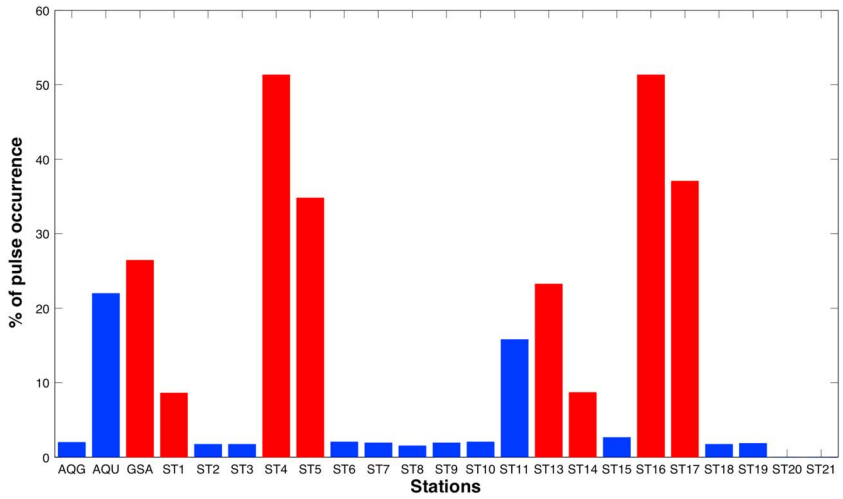

Figure 7. Description of the spatial distribution pulse emergence. The histogram shows the percentage of pulse occurrence at the stations of Figure 3. Footwall stations (marked with red bars) show more pulses than hanging wall stations (marked with blue bars).

with the 75th percentile of the distribution in Figure 8b corresponding to four stations (~17% of the stations) and the 95th percentile to seven stations (~30%). Finally, from the distribution in Figure 8b, the average number of stations presenting an impulsive behavior is 2.8 (~12% of the stations) with a standard deviation of 2.1.

In Figure 8b the histogram shows the number of events as a function of the number of stations at which these events have produced an impulsive ground motion.

We also reanalyzed the dependence on the risetime, showing the pulse duration as a function of the source-receiver epicentral distance and the rupture speed. In Figure 9a, the pulse duration and its standard deviation are shown for the station AQU, grouping the results in distance bins; the different colors refer to the simulations carried out by imposing the risetime values τ = 0.6, 0.9, and 1.2 s, respectively. The pulse duration increases as the epicentral distance increases, this latter being connected to the distance covered by the rupture under directive regime. In Figure 9b, we plot the pulse size as a function of the rupture velocity at the same station. Increasing the rupture speed reduces the duration of the coherent radiation contribution under directive regime and diminishes the final duration of the pulses. In Figures 9c and 9d the same plots are

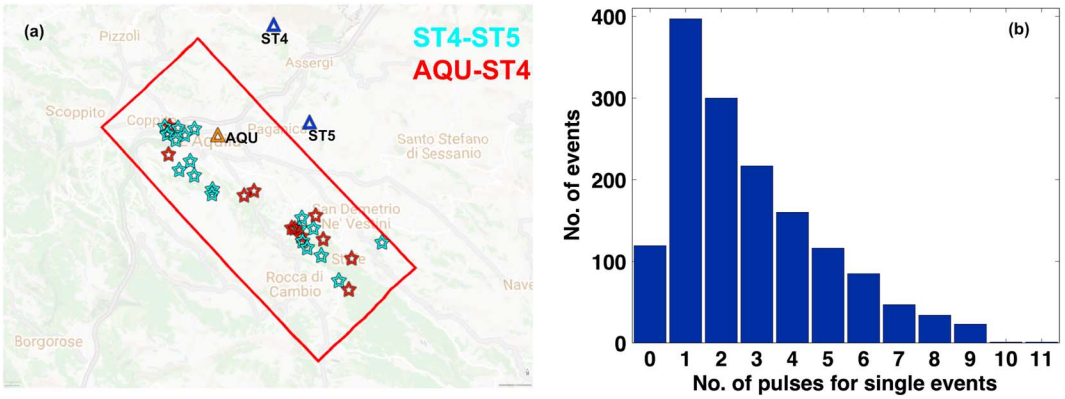

Figure 8. Figure 8a shows the distribution of the epicenters of the events that produce pulses only at ST4-ST5 (cyan stars) and at AQU-ST4 (red stars). In the former case, we can individuate two clusters: Events are either located at large depth on the same half-side of the fault or on the other side at shallower depth. In the latter case, events originate on the south-east part of the fault and generate pulses as a combination of the along-dip and along-strike directivity.

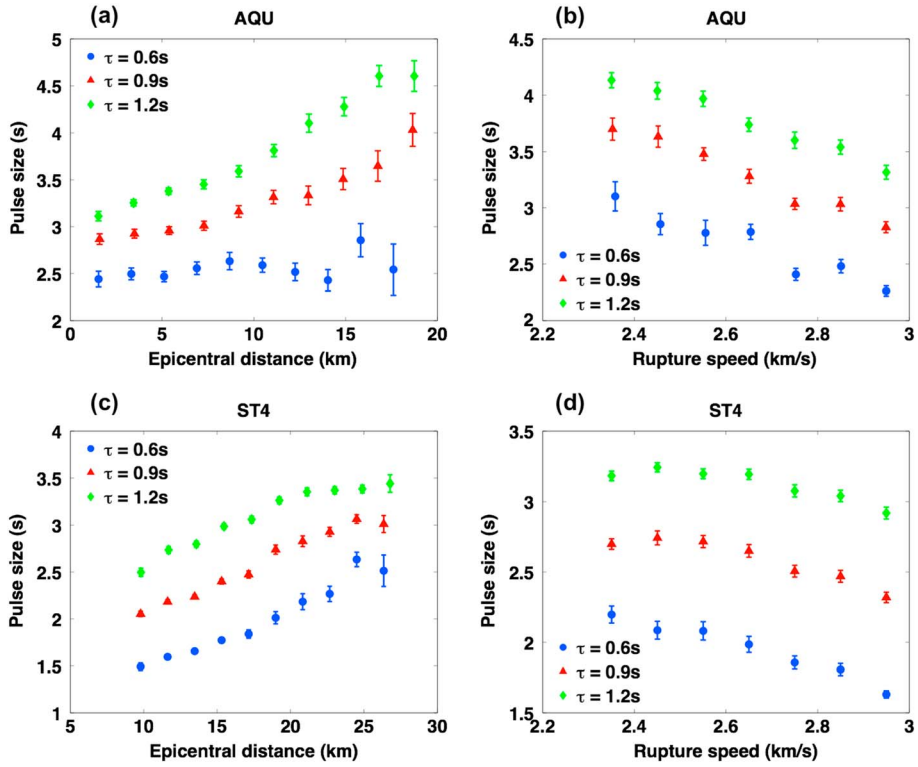

Figure 9. Variability of the pulse durations as a function of some source features. Pulse duration versus epicentral distance for the hanging wall station AQU (a) and the footwall station ST4 (c). Pulse versus rupture speed for the hanging wall station AQU (b) and the footwall station ST4 (d). In all panels the different colors represent the results achieved for different risetime, as clarified in the legend.

shown for the footwall station ST4, which experienced the largest frequency of pulse occurrence. The trends of the pulse duration with the distance and the rupture velocity are similar to AQU, even though the correlation is less pronounced. The effect of the risetime results at the first order as an additive term not modifying the qualitative trend of the relationships. The apparent dissimilarity in the trend of Figure 9a is likely due to the scarce number of detected pulses for small risetime values making the statistics less robust. We also found that the duration is almost insensitive to the slip roughness. Longer pulse durations (>3 s) occur when the hypocenter is on the opposite side of the fault as compared to the receiver location, and the pulses are due to the coupling between updip and along-strike directivity effects.

In order to evaluate the intraevent pulse duration variability, we considered the ensemble of synthetic data carried out with τ = 0.6 s. The average duration is 2.4 s with a standard deviation of 0.6 s. We compare this value with the estimates extracted from Baker (2007) for a M_w = 6.3 earthquake, which are 1.9 and 1.0 s for the mean and the standard deviation, respectively. We note that the mean value retrieved in this study is compatible with the estimate of Baker (2007), which combines data from earthquakes recorded in different tectonic regimes. We finally computed the standard deviation around the average pulse size for all the 684 events showing pulses at least at three stations. The average of these 684 standard deviations is used as an estimate of the intraevent variability, and it is σ_t = 0.54 s, this value being lower than the standard deviation estimated by the Baker scaling law.

5. Discussion

The main effect in the spatial distribution of the pulse occurrence and duration is related to the location of the station with respect to the fault, if it lies on the hanging wall or on the footwall.

In particular, the footwall stations experience on average a frequency of the pulse occurrence that is more than twice larger than the average for the hanging wall stations.

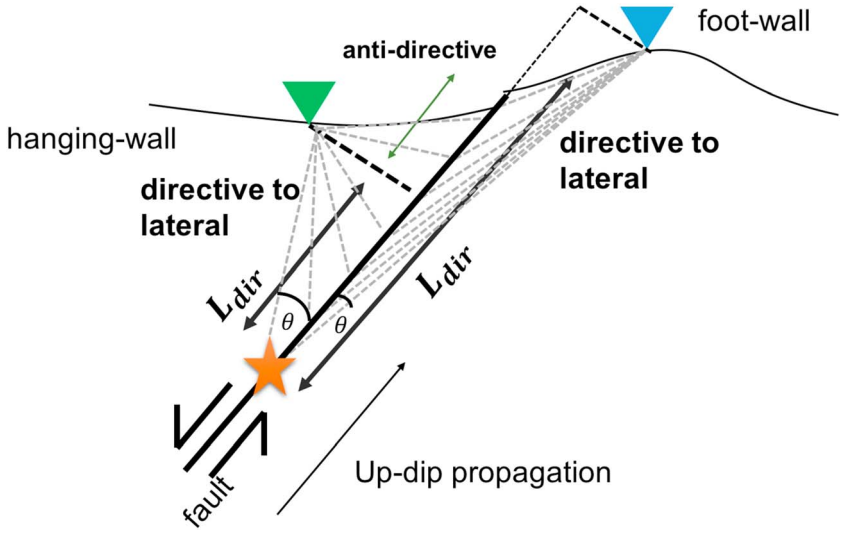

Figure 10. The plot provides an interpretation of the higher pulse occurrence on the footwall stations. These latter stations (cyan triangle) see as directive all the updip propagation along all the direction over the fault plane. This contributes to give coherency to the emitted signals during the rupture propagation and to concentrate the most part of the energy in small part of the recorded seismograms. Conversely, when a station is on the hanging wall (green triangle), there is always a point (the base of the dashed black line on the left side) after which the propagation is seen as antidirective by the station itself. This eventually subtracts coherency to the emitted radiation spreading the energy in the seismograms over longer time intervals.

This larger pulse occurrence in the footwall is a consequence of the updip directivity effect as illustrated in Figure 10. Whatever is the depth of the nucleation and the position of the station on the footwall (see the cyan triangle in the Figure 10) the updip propagation of the rupture will be seen from that station as entirely directive. On the contrary, a station on the hanging wall (see the green triangle in the Figure 10) experiences a transition from a directive position to an antidirective one after the rupture overcomes the projection of the station on the fault (dashed black line on the left side in Figure 10), contributing to enlarge the signal coda duration and thus limiting the pulse emergence. We also expect larger pulse duration in the footwall than in the hanging wall. Additionally, impulsive ground motion may be due to the combination of along-strike and along-dip directivity, with the coupling more pronounced for the hanging wall stations than for the footwall ones.

We observed that the duration of the impulsive ground motion is increasing with the hypocentral distance and decreasing with the rupture velocity, while the risetime appears as an additive contribution to the first order. The Doppler effect can be used to model the impulsive signal duration as observed from the numerical simulations, using the simplified sketch of Figure 10. Assuming a constant rupture velocity v_r and a homogeneous medium with S wave velocity v_s, the expected duration of the pulse T_p^e is (Fayjaloun et al., 2017)

$$T_p^e \approx \tau + \frac{L_{\mathrm{dir}}}{v_r} - \frac{1}{v_s}\int_0^{L_{\mathrm{dir}}} \cos\theta(x)dx \approx \tau + \frac{L_{\mathrm{dir}}}{v_r} - \frac{L_{\mathrm{dir}}}{v_s}\cos\theta_0 \tag{2}$$

where τ is the constant risetime on the fault and the angle θ is plotted in Figure 10 both for the hanging wall and footwall stations with the subscript zero referring to the hypocenter.

L_{dir} is the distance covered by the rupture in the directive regime, which generally combines along-dip and along-strike directivity, as it is the distance between the hypocenter and the projection of the station onto the fault surface for a hanging wall station and the distance from the hypocenter to the point of the fault closest to the receiver for the footwall stations. Thus, it is equivalent to the parameter d defined in Shahi and Baker (2011). A representation of the quantity L_{dir} is shown by a double arrow in Figure 10 both for the hanging wall and footwall. Figure 11a shows the comparison between the pulse duration T_p^o computed from the simulations (red dots) and the theoretical duration T_p^e (blue dots) from equation (2), using the source parameters that have generated impulsive synthetic ground motion at the hanging wall station AQU. In Figure 11b

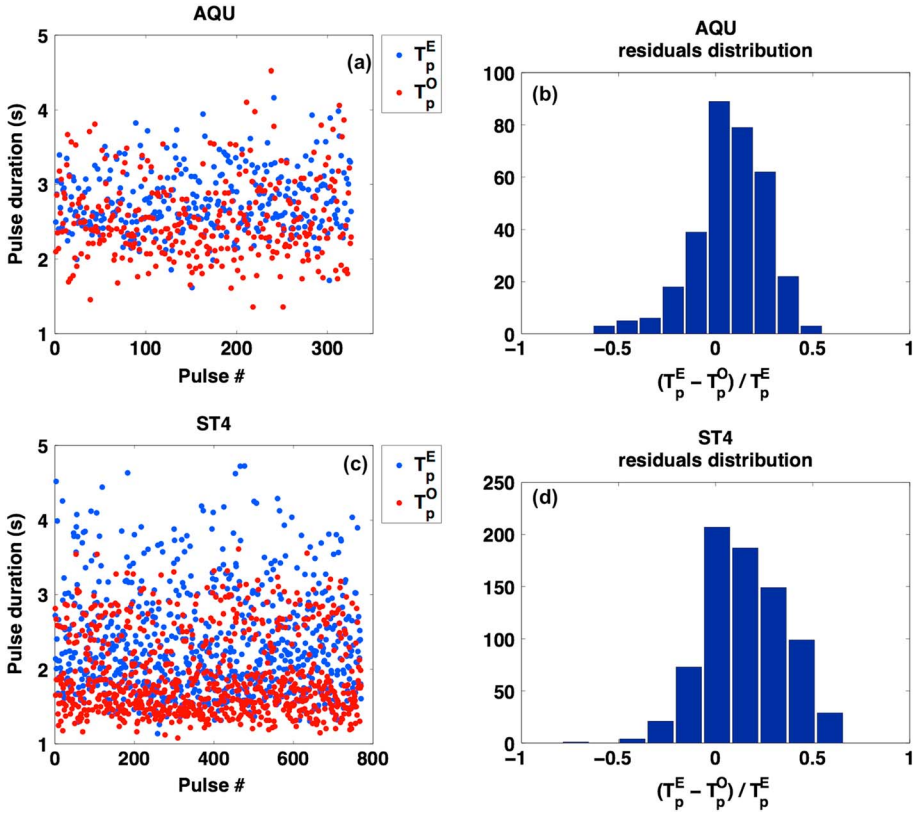

Figure 11. For the same stations of Figure 9, we show the distribution of the residuals between the theoretical and the computed pulse duration from synthetics. In Figure 11a the blue and red dots represent, respectively, T_p^E and T_p^O at the hanging wall station AQU, whereas in Figure 11b the normalized residuals are grouped in bins. In Figures 11c and 11d similar results are shown for the footwall station ST4.

the histogram of the normalized residuals $\left(T_p^e - T_p^o\right)/T_p^e$ is plotted. The distribution has a mean value $\mu = 0.07$ and a standard deviation $\sigma = 0.19$ evidencing a good agreement between the expected and the observed pulse duration. Figures 11c and 11d show a similar result for the footwall station ST4 with the distribution of the residuals having a mean value $\mu = 0.15$ and a standard deviation $\sigma = 0.20$. The slight overestimate of the expected pulse size can be due to the simplicity of the one-dimensional model that does not take into account at all the complexity of the source model introduced by the k^{-2} slip distributions. Nevertheless, Figures 11b–11d show that for both cases the modal class of the distribution contains the zero. Finally, using the same correlation estimator of Fayjaloun et al. (2017), that is, the natural logarithm residuals, we obtain $\sigma_{\ln T(\mathrm{AQU})} = 0.20$ and $\sigma_{\ln T(\mathrm{ST4})} = 0.26$ for AQU and ST4, respectively, improving the previous estimate.

A final comment is related to the station AQG. At this station a short duration pulse signal (~1.0 s) was observed during the 6 April 2009, L'Aquila earthquake (Chioccarelli & Iervolino, 2010). Nevertheless, occurrence of pulse-like signals at this station is very rare in our numerical simulations and the pulse never emerges when the hypocenter location is very close to the real one. We suggest that the real source geometry is more complex beneath AQG than the one we assumed in our simulations, with possible changes in the focal mechanism close to the north boundary of the fault. This will allow energy focusing and possibly directivity effects also at AQG.

6. Conclusions

We performed kinematic simulations of seismic ruptures assuming a L'Aquila-like source model and a k^{-2} description of the rupture process. We investigated the sensitivity of the kinematic parameters to the pulse emergence and duration. We found that the emergence of the pulse is not dependent on the variability of

the risetime on the fault, but its emergence and duration depend on the average value of the risetime, on the station position, on the rupture speed, on the event depth, and less significantly on the slip roughness. Specifically, stations on the footwall experience a large number of pulses with longer duration, as compared to receivers in the hanging wall as an effect of the updip directivity. As the rupture speed increases, the signal becomes shorter, and the emergence of pulses is enhanced while its duration decreases. We modeled the pulse duration using a simplified 1-D Doppler model as shown in equation (2). The good agreement between the model and the computed duration from synthetics has been shown in terms of residuals.

When analyzing the intraevent pulse occurrence, we observe that the average percentage of stations where the pulse occurs is ~ 12%, when a uniform station coverage around the fault is available. In all cases, stations located on the hanging wall in the opposite direction, as compared to the updip propagation, almost never experience any pulse. The average intraevent variability of the pulse size is about 0.5 s, this value being smaller than the standard deviation expected from the scaling law proposed by Baker (2007) for that magnitude.

Acknowledgments
The authors acknowledge Georgios Baltzopoulos and Iunio Iervolino for fruitful scientific discussions about the topics of this work. The authors also akcnowledge projects RELUIS-DPC and SERA for supporting the activity. RELUIS-DPC is a national project, supported by the Department of Civil Protection; SERA has received funding from the European Union's HORIZON 2020 with the project ID 730900. The data for this paper can be accessed at the doi: 10.6084/m9.figshare.6406448.

References

Abercrombie, R. E., Poli, P., & Bannister, S. (2017). Earthquake directivity, orientation, and stress drop within the subducting plate at the Hikurangi margin, New Zealand. *Journal of Geophysical Research: Solid Earth*, *122*, 10,176–10,188. https://doi.org/10.1002/2017JB014935

Akkar, S., & Bommer, J. J. (2010). Empirical equations for the prediction of PGA, PGV and spectral accelerations in Europe, the Mediterranean region and the Middle East. *Seismological Research Letters*, *81*(2), 195–206. https://doi.org/10.1785/gssrl.81.2.195

Alavi B., & Krawinkler H. (2001). Effects of near-fault ground motions on frame structures, in Report no. 138, February 2001, Department of Civil and Enviromental Engineering Stanford University.

Ameri, G., Gallovic, F., & Pacor, F. (2012). Complexity of the Mw 6 3 2009 L'Aquila (central Italy) earthquake: 2 broadband strong motion modeling. *Journal of Geophysical Research*, *117*, B04308. https://doi.org/10.1029/2011JB008729

Baker, J. W. (2007). Quantitative classification of near-fault ground motions using wavelet analysis. *Bulletin of the Seismological Society of America*, *97*(5), 1486–1501. https://doi.org/10.1785/0120060255

Baker, J. W., Lin T., Shahi S. K., & Jayaram N. (2011). New ground motion selection procedures and selected motions for the PEER transportation research program. PEER Technical Report 2011/03.106p.

Baltzopoulos, G., Vamvatsikos, D., & Iervolino, I. (2016). Analytical modelling of near-source pulse-like seismic demand for multi-linear backbone oscillators. *Earthquake Engineering and Structural Dynamics*, *45*(11), 1797–1815. https://doi.org/10.1002/eqe.2729

Bernard, P., Herrero, A., & Berge, C. (1996). Modeling directivity of heterogeneous earthquake ruptures. *Bulletin of the Seismological Society of America*, *86*, 1149–1160.

Bernard, P., & Madariaga, R. (1984a). High frequency radiation from a buried circular crack. *Geophysical Journal of the Royal Astronomical Society*, *78*(1), 1–17. https://doi.org/10.1111/j.1365-246X.1984.tb06468.x

Bernard, P., & Madariaga, R. (1984b). A new asymptotic method for the modeling of near-field accelerograms. *Bulletin of the Seismological Society of America*, *74*, 539–557.

Bianchi, I., Chiarabba, C., & Piana Agostinetti, N. (2010). The 2009 L'Aquila (central Italy) earthquake rupture controlled by a high vs barrier: A receiver function application. *Journal of Geophysical Research*, *115*, B12326. https://doi.org/10.1029/2009JB007087

Boatwright, J., & Boore, D. M. (1982). Analysis of the ground accelerations radiated by the 1980 Livermore Valley earthquakes for directivity and dynamic source characteristics. *Bulletin of the Seismological Society of America*, *72*, 1843–1865.

Bray, J. D., & Rodriguez-Marek, A. (2004). Characterization of forward-directivity ground motions in the near-fault region. *Soil Dynamics and Earthquake Engineering*, *24*(11), 815–828. https://doi.org/10.1016/j.soildyn.2004.05.001

Burridge, R. (1973). Admissible speeds for plane-strain self-similar shear cracks with friction but lacking cohesion. *Geophysical Journal of the Royal Astronomical Society*, *35*(4), 439–455. https://doi.org/10.1111/j.1365-246X.1973.tb00608.x

Calderoni, G., Rovelli, A., Ben-Zion, Y., & Di Giovambattista, R. (2015). Along-strike rupture directivity of earthquakes of the 2009 L'Aquila, central Italy, seismic sequence. *Geophysical Journal International*, *203*(1), 399–415. https://doi.org/10.1093/gji/ggv275

Causse, M., Chaljub, E., Cotton, F., Cornou, C., & Bard, P. Y. (2009). New approach for coupling k^{-2} and empirical Green's functions: Application to the blind prediction of broadband ground-motion in the Grenoble Basin. *Geophysical Journal International*, *179*(3), 1627–1644. https://doi.org/10.1111/j.1365-246X.2009.04354.x

Chiarabba, C., Amato, A., Anselmi, M., Baccheschi, P., Bianchi, I., Cattaneo, M., et al. (2009). The 2009 L'Aquila (central Italy) M_W6.3 earthquake: Main shock and aftershocks. *Geophysical Research Letters*, *36*, L18308. https://doi.org/10.1029/2009GL039627

Chioccarelli, E., & Iervolino, I. (2010). Near-source seismic demand and pulse-like records: A discussion for L'Aquila earthquake. *Earthquake Engineering and Structural Dynamics*, *39*(9), 1039–1062. https://doi.org/10.1002/eqe.987

Chioccarelli, E., & Iervolino, I. (2013). Near-source seismic hazard and design scenarios. *Earthquake Engineering and Structural Dynamics*, *42*(4), 603–622. https://doi.org/10.1002/eqe.2232

Cirella, A., Piatanesi, A., Cocco, M., Tinti, E., Scognamiglio, L., Michelini, A., et al. (2009). Rupture history of the 2009 L'Aquila earthquake from non-linear joint inversion of strong motion and GPS data. *Geophysical Research Letters*, *36*, L19304. https://doi.org/10.1029/2009GL039795

Cirella, A., Piatanesi, A., Tinti, E., Chini, M., & Cocco, M. (2012). Complexity of the rupture process during the 2009 L'Aquila, Italy, earthquake. *Geophysical Journal International*, *190*(1), 607–621. https://doi.org/10.1111/j.1365-246X.2012.05505.x

Cork, T. G., Kim, J. H., Mavroeidis, G. P., Kim, J. K., Halldorsson, B., & Papageorgiou, A. S. (2016). Effects of tectonic regime and soil conditions on the pulse period of near-fault ground motions. *Soil Dynamics and Earthquake Engineering*, *80*, 102–118. https://doi.org/10.1016/j.soildyn.2015.09.011

Coutant, O. (1989). Programme de simulation numérique AXITRA. in Rapport LGIT. Université Joseph Fourier, Grenoble, France.

Cultrera, G., Pacor, F., Franceschina, G., Emolo, A., & Cocco, M. (2009). Directivity effects for moderate-magnitude earthquakes (Mw 5.6–6.0) during the 1997 Umbria-Marche sequence, central Italy. *Tectonophysics*, *476*(1-2), 110–120. https://doi.org/10.1016/j.tecto.2008.09.022

Del Gaudio, S., Festa, G., & Causse, M. (2015). Strong motion numerical simulations using the empirical Green's function method: Application to 2009 L'Aquila earthquake. *Geophysical Journal International*, *203*(1), 720–736. https://doi.org/10.1093/gji/ggv325

Evangelista, L., Del Gaudio, S., Smerzini, C., D'Onorio, A., Festa, G., Iervolino, I., et al. (2017). Physics-based seismic input for engineering applications: A case study in the Aterno River valley, Central Italy. *Bulletin of Earthquake Engineering*, *15*(7), 2645–2671. https://doi.org/10.1007/s10518-017-0089-7

Fayjaloun, R., Causse, M., Voisin, C., Cornou, C., & Cotton, F. (2017). Spatial variability of the directivity pulse periods observed during an earthquake. *Bulletin of the Seismological Society of America*, *107*(1), 308–318. https://doi.org/10.1785/0120160199

Gallovic, F., & Zahradnık, J. (2011). Complexity of the M6.3 2009 L'Aquila (central Italy) earthquake: 1. Multiple finite-extent source inversion. *Journal of Geophysical Research*, *117*, B04307. https://doi.org/10.1029/2011JB008709

Geller, R. J. (1976). Scaling relations for earthquake source parameters and magnitudes. *Bulletin of the Seismological Society of America*, *66*(5), 1501–1523.

Hanks, C. T., & McGuire, R. K. (1981). The character of high-frequency strong ground motion. *Bulletin of the Seismological Society of America*, *71*(6), 2071–2095.

Herrero, A., & Bernard, P. (1996). Modeling directivity of heterogeneous earthquake ruptures. *Bulletin of Seismological Society of America*, *86*(4), 1149–1160.

Hubbard, D. T., & Mavroeidis, G. P. (2011). Damping coefficients for near-fault ground motion response spectra. *Soil Dynamics and Earthquake Engineering*, *31*(3), 401–417. https://doi.org/10.1016/j.soildyn.2010.09.009

Iervolino, I., Baltzopoulos, G., & Chioccarelli, E. (2016). Preliminary engineering analysis of the August 24th 2016, ML 6.0 central Italy earthquake records. *Annals of Geophysics*, *59*, 1–9. https://doi.org/10.4401/ag-7182

Iervolino, I., Baltzopoulos, G., Chioccarelli, E., & Suzuki, A. (2017). Seismic actions on structures in the near-source region of the 2016 central Italy sequence. *Bulletin of Earthquake Engineering*, 1–19. https://doi.org/10.1007/s10518-017-0295-3

Iervolino, I., Chioccarelli, E., & Baltzopoulos, G. (2012). Inelastic displacement ratio of near-source pulse-like ground motions. *Earthquake Engineering and Structural Dynamics*, *41*, 2351–2357. https://doi.org/10.1002/eqe.2167

Iervolino, I., & Cornell, C. A. (2008). Probability of occurrence of velocity pulses in near-source ground motions. *Bulletin of the Seismological Society of America*, *98*(5), 2262–2277. https://doi.org/10.1785/0120080033

Kane, D. L., Shearer, P. M., Goertz-Allmann, B. P., & Vernon, F. L. (2013). Rupture directivity of small earthquakes at Parkfield. *Journal of Geophysical Research: Solid Earth*, *118*, 1–10. https://doi.org/10.1029/2012JB009675

Kurzon, I., Vernon, F. L., Ben-Zion, Y., & Atkinson, G. (2014). Ground motion prediction equations in the San Jacinto fault zone: Significant effects of rupture directivity and fault zone amplification. *Pure and Applied Geophysics*, *171*(11), 3045–3081. https://doi.org/10.1007/s00024-014-0855-2

Liossatu, E., & Fardis, M. N. (2016). Near-fault effects on residuals displacements of RC structures. *Earthquake Engineering and Structural Dynamics*, *45*(9), 1391–1409.

Luo, Y., Tan, Y., Wei, S., Helmberger, D., Zhan, Z., Ni, S., et al. (2010). Source mechanism and rupture directivity of the 18 May 2009 M_w 4.6 Inglewood, California earthquake. *Bulletin of Seismological Society of America*, *100*(6), 3269–3277. https://doi.org/10.1785/0120100087

Luzi, L., Puglia, R., Russo, E., D'Amico, M., Felicetta, C., Pacor, F., et al. (2016). The engineering strong motion database: A platform to access pan-European accelerometric data. *Seismological Research Letters*, *87*(4), 987–997. https://doi.org/10.1785/0220150278

Mai, P. M., & Thingbaijam, K. K. S. (2014). SRCMOD: An online database of finite-fault rupture models. *Seismological Research Letters*, *85*(6), 1348–1357. https://doi.org/10.1785/0220140077

Mavroeidis, G. P., & Papageorgiou, A. S. (2003). A mathematical representation of near-fault ground motions. *Bulletin of the Seismological Society of America*, *93*(3), 1099–1131. https://doi.org/10.1785/0120020100

Mavroeidis, G. P., & Papageorgiou, A. S. (2010). Effect of fault rupture characteristics on near-fault strong ground motions. *Bulletin of the Seismological Society of America*, *100*(1), 37–58. https://doi.org/10.1785/0120090018

Rice, J. R. (1979). The mechanics of earthquake rupture. In A. M. Dziewonski & E. Boschi (Eds.), *Physics of the Earth's Interior, course, Proceedings to the International School of Physics "Enrico Fermi"* (Vol. 78, pp. 555–649). Varenna, Lake Como.

Rubin, A. M., & Ampuero, J.-P. (2007). Aftershock asymmetry on a bimaterial interface. *Journal of Geophysical Research*, *112*, B05307. https://doi.org/10.1029/2006JB004337

Ruiz-Garcia, J. (2011). Inelastic displacement ratios for seismic assessment of structures subjected to forward-directivity near-fault ground motions. *Journal of Earthquake Engineering*, *15*(3), 449–468. https://doi.org/10.1080/13632469.2010.498560

Sabetta, F., & Pugliese, A. (1996). Estimation of response spectra and simulation of non-stationary earthquake ground motions. *Bulletin of the Seismological Society of America*, *86*, 337–352.

Sato, R. (1979). Theoretical basis on relationships between focal parameters and earthquake magnitude. *Journal of Physics of the Earth*, *27*(5), 353–372. https://doi.org/10.4294/jpe1952.27.353

Scala, A., Festa, G., & Vilotte, J.-P. (2017). Rupture dynamics along bimaterial interfaces: A parametric study of the shear-normal traction coupling. *Geophysical Journal International*, *209*(1), ggw489–ggw467. https://doi.org/10.1093/gji/ggw489

Shahi, S. K., & Baker, J. W. (2011). An empirically calibrated framework for including the effects of near-fault directivity in probabilistic seismic hazard analysis. *Bulletin of Seismological Society of America*, *101*(2), 742–755. https://doi.org/10.1785/0120100090

Smerzini, C., & Villani, M. (2012). Broadband numerical simulations in complex near-field geological configurations: The case of the Mw 6.3 2009 L'Aquila earthquake. *Bulletin of the Seismological Society of America*, *102*(6), 2436–2451. https://doi.org/10.1785/0120120002

Somerville, P. G., Smith, N. F., Graves, R. W., & Abrahamson, N. A. (1997). Modification of empirical strong motion attenuation relations to include the amplitude and duration effect of rupture directivity. *Seismological Research Letters*, *68*(1), 199–222. https://doi.org/10.1785/gssrl.68.1.199

Sommerville, P. G. (2003). Magnitude scaling of the near fault rupture directivity pulse. *Physics of the Earth and Planetary Interiors*, *137*(1-4), 201–212. https://doi.org/10.1016/S0031-9201(03)00015-3

Sommerville P. G. (2005). *Engineering characterization of near fault ground motions*. Paper presented at 2005 NZSEE Conference, Taupo, New Zealand.

Spudich, P., & Chiou, B. S. J. (2008). Directivity in NGA earthquake ground motions: Analysis using Isochrone theory. *Earthquake Spectra*, *24*(1), 279–298. https://doi.org/10.1193/1.2928225

Tothong, P., Cornell, A. C., & Baker, J. W. (2007). Explicit directivity-pulse inclusion in probabilistic seismic hazard analysis. *Earthquake Spectra*, *23*(4), 867–891. https://doi.org/10.1193/1.2790487

Tothong, P., & Luco, N. (2007). Probabilistic seismic demand analysis using advanced ground motion intensity measures. *Earthquake Engineering and Structural Dynamics*, *36*(13), 1837–1860. https://doi.org/10.1002/eqe.696

Erratum

In the originally published version of this article, there was an error in Figure 1. The error has been corrected, and this version may be considered the authoritative version of record.